NANO LETTERS

Letter

pubs.acs.org/NanoLett

Graphene-Based Thermopile for Thermal Imaging Applications

Allen L. Hsu,[†] Patrick K. Herring,[‡,∥] Nathaniel M. Gabor,[⊥] Sungjae Ha,[†] Yong Cheol Shin,[§] Yi Song,[†] Matthew Chin,[#] Madan Dubey,[#] Anantha P. Chandrakasan,[†] Jing Kong,[†] Pablo Jarillo-Herrero,[*,‡] and Tomás Palacios[*,†]

[†]Department of Electrical Engineering and Computer Science, [‡]Department of Physics, and [§]Department of Materials Science and Engineering, Massachusetts Institute of Technology, Cambridge, Massachusetts 02139, United States

[∥]Department of Physics, Harvard University, Cambridge, Massachusetts 02138, United States

[⊥]Department of Physics and Astronomy, University of California, Riverside, Riverside, California 92521, United States

[#]Army Research Laboratory, 2800 Powder Mill Road, Adelphi, Maryland 20783, United States

Supporting Information

ABSTRACT: In this work, we leverage graphene's unique tunable Seebeck coefficient for the demonstration of a graphene-based thermal imaging system. By integrating graphene based photothermo-electric detectors with micromachined silicon nitride membranes, we are able to achieve room temperature responsivities on the order of ~7–9 V/W (at λ = 10.6 μm), with a time constant of ~23 ms. The large responsivities, due to the combination of thermal isolation and broadband infrared absorption from the underlying SiN membrane, have enabled detection as well as stand-off imaging of an incoherent blackbody target (300–500 K). By comparing the fundamental achievable performance of these graphene-based thermopiles with standard thermocouple materials, we extrapolate that graphene's high carrier mobility can enable improved performances with respect to two main figures of merit for infrared detectors: detectivity (>8 × 10^8 cm $Hz^{1/2}$ W^{-1}) and noise equivalent temperature difference (<100 mK). Furthermore, even average graphene carrier mobility (<1000 cm^2 V^{-1} s^{-1}) is still sufficient to detect the emitted thermal radiation from a human target.

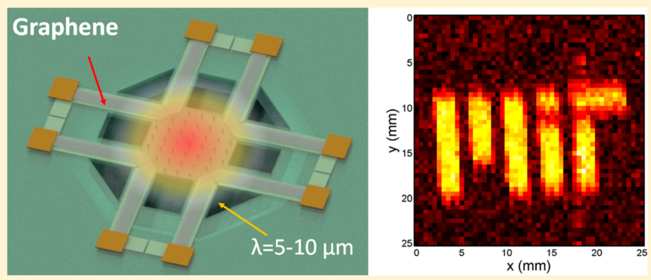

KEYWORDS: *Graphene, thermal imaging, infrared, detectors, thermopile, microelectromechanical Systems*

Detectors sensitive in the infrared (λ = 5–15 μm) have a large range of applications from infrared thermography, chemical spectroscopy, and active night vision systems.[1] Graphene, due to its symmetric conical band structure and broad band optical absorption, has recently been explored as a new material for infrared photon-based detectors.[2−7] Current technologies, such as high performance photon based detectors (i.e., HgCdTe), often require cryogenic cooling to mitigate noise sources such as thermally excited carriers or stray blackbody optical photons. These drawbacks can be avoided at infrared wavelengths by using thermal detectors that offer higher sensitivities at 300 K. Therefore, in this work we leverage graphene's band structure not for optical detection but rather thermal detection in the mid-infrared.[8−14] By integrating graphene-based ambipolar thermopiles with silicon micro-electro-mechanical (MEMS) structures, we are able to perform thermal imaging of a blackbody source, achieving sensitivities able to detect the emitted radiation from a human hand. Analysis shows the ultrahigh carrier mobility of graphene can enable intrinsic performances surpassing state-of-the-art thermopile imagers, potentially enabling new classes of low cost, transparent, and flexible thermal imagers.

Thermal infrared detectors rely upon radiative heat transfer between the image object and the detector in order to measure small changes in temperature.[15−18] This transduction mechanism can take many forms such as temperature-dependent change in resistance (bolometer)[10,13,14] or thermally generated voltage via the Seebeck effect (thermopiles).[11,19] In the case of our device, we leverage the latter effect using a graphene based ambipolar thermocouple as the thermal readout device.[8,19,20] By developing a graphene compatible wafer scale MEMS process, we are able to thermally isolate our devices and demonstrate high sensitivity thermal detection and imaging. Figure 1a shows the graphene–MEMS integration process (see Supporting Information for more details). Utilizing the underlying silicon substrate as a sacrificial release material in conjunction with a protective poly methyl-methacrylate (PMMA) layer for the graphene, we are able to release the membrane (100 nm SiO_2/500 nm SiN/100 nm SiO_2) and the graphene without the need for any wet chemical processes. The completed device diagram and optical picture of the graphene thermopile are shown in Figure 1b,c, respectively. To increase the thermal absorption area, graphene thermocouples are placed at the periphery of the central

Received: May 4, 2015
Revised: October 6, 2015
Published: October 15, 2015

DOI: 10.1021/acs.nanolett.5b01755
Nano Lett. 2015, 15, 7211−7216

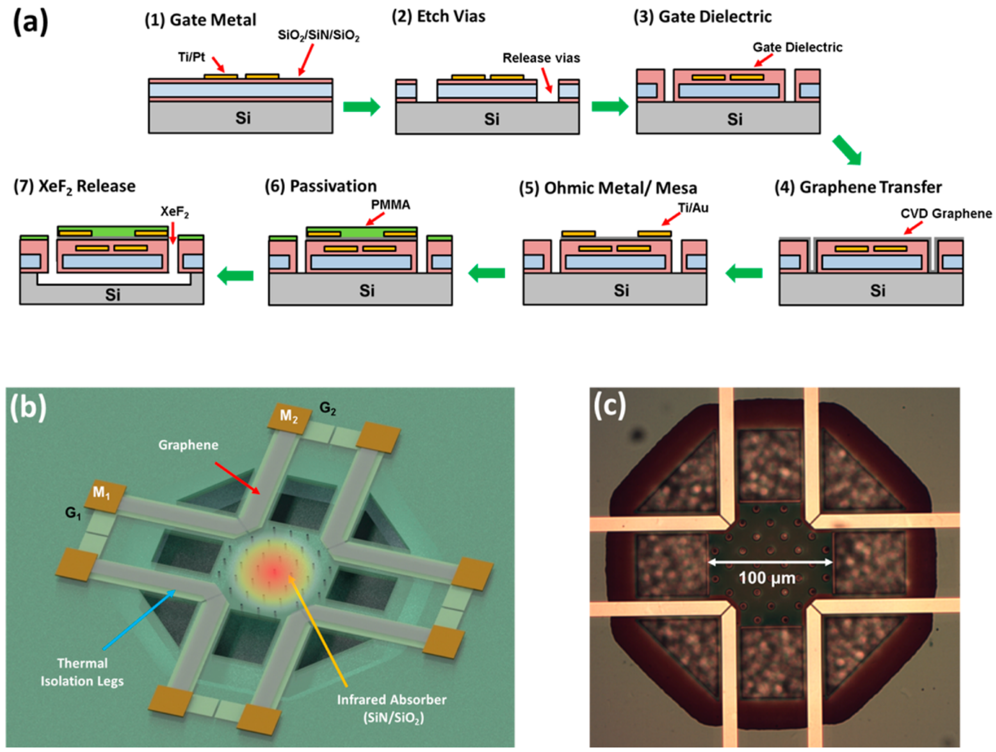

Figure 1. (a) Graphene thermopile fabrication flow and schematic process flow. Starting wafer consists of thermal isolation stack of SiO_2/SiN/SiO_2 (100 nm/500 nm/100 nm) deposited by plasma-enhanced chemical vapor deposition (PE-CVD) on top of a standard Si wafer. (1) Electron-beam evaporation of the gate metal, Ti/Pt (10 nm/20 nm). (2) Plasma etching through the thermal isolation layer using CF_4. (3) Gate dielectric deposition of 80 nm SiO_2 by PE-CVD. (4) Wet transfer of CVD graphene. (5) Ohmic metal deposition, Ti/Au (1 nm/30 nm) and graphene electrical isolation by reactive oxygen etching. (6) Passivation of graphene using poly methyl-methacrylate (PMMA). (7) Suspension of thermal isolation layer using XeF_2 to etch underlying silicon. (b) Schematic of graphene thermopile. Note that wire bonding pads are not shown. Small holes in the center of the infrared absorber are meant to facilitate suspension of the thermal isolation stack, while the large openings along the periphery help define the thermal isolation legs. (c) Optical micrograph of the completed device. Central infrared absorbing region is 100 μm.

suspended absorber (SiN: 100 μm × 100 μm). The graphene traverses between the cold (substrate supported side) and hot reservoirs (the suspended SiN membrane side) through the thermal isolation legs (L = 64 μm, W = 16 μm). Arrays of these graphene thermopiles are fabricated simultaneously, each containing four graphene ambipolar thermocouple junctions. The fully packaged thermopile consists of two pairs of bond pads (outside the field of view in Figure 1c) for wire bonding to the individual gates (V_{G1} and V_{G2}) and terminals (V_{M1} and V_{M2}) of the device. Multiple thermocouples can be measured in series for multijunction measurements through external wiring of selected thermocouples (details of device characterization can be found in the Supporting Information). The room temperature electrical resistance (R) and open-circuit photovoltage (V_{PH}) from a two junction device, as a function of gate voltage (measured under vacuum), are shown in Figure 2a,b. The graphene is slightly p-type doped with a maximum resistance occurring at V_{G1} = +10 V and V_{G2} = +20 V and a field effect mobility (μ) of ~86 cm^2 V^{-1} s^{-1}. The open-circuit photovoltage (V_{PH}) response from our detector was measured with a CO_2 laser input (P = 280 μW), while varying V_{G1} and V_{G2} simultaneously (Figure 2b). The measured V_{PH} shows distinctive changes in polarity due to the tunable Seebeck coefficient of graphene. Figure 2c shows the measured voltage responsivity (R_V) of our devices as a function of optical modulation frequency (f_{mod}). At low modulation speeds (f_{mod} < 30 Hz), the devices achieved an R_V of 7−9 V/W, with a thermal time constant (τ_{th}) of 23 ms (see Supporting Information). Compared to our previous devices, this >1000× improvement in responsivity is consistent with the thermal engineering of our isolated SiN membrane (see Supporting Information).[21] The inset in Figure 2c shows the broadband infrared transmission (τ_{SiN}) of the SiN membrane, which only absorbs ~50% of the incident light at λ = 10.6 μm suggesting even larger responsivities are possible (see Supporting Information).

However, due to the already drastic improvement in responsivity, demonstration of active thermal imaging using graphene is now possible. While many previous works utilized narrow line width and high intensity laser sources (~mW),[8,22] in this work optical detection of a low power, incoherent, broadband blackbody source (Omega − 1″ diameter) is achieved, mimicking the properties of real-world thermal sources. Figure 3a shows our device characterization system for coupling the incident blackbody source with our detector (see Supporting Information). The V_{PH} (f_{mod} = 173 Hz, integration time (τ_{int}) = 1s) of a single graphene thermocouple was measured as a function of increasing blackbody temperature (T_0) from 372 to 534 K with the device at room temperature and under vacuum. As expected from Planck's law for an ideal blackbody source ($P \propto T_0^4$), the measured photovoltage response of our devices ($V_{PH} \propto T_0^{4.344}$) follows a similar relationship. To perform active thermal imaging, a thermal target is placed in the imaging plane of IM1 (Figure 3c). Due to the packaging of the device inside of the cryostat, the thermal image was scanned across IM1 rather than scanning the position of the detector, which given the one-to-one mapping between conjugate image planes are equivalent operations. The thermal image was a stainless steel

DOI: 10.1021/acs.nanolett.5b01755
Nano Lett. 2015, 15, 7211−7216

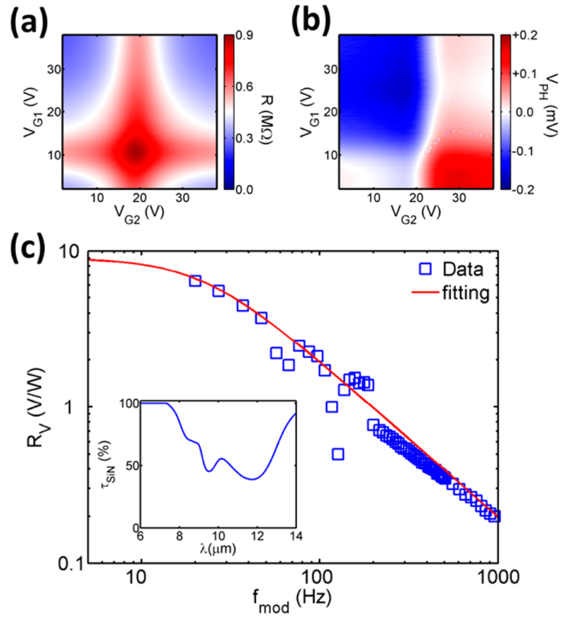

Figure 2. Electrical and optical characterization of the graphene thermopile. (a) Resistance of the graphene thermopile (number of junctions = 2) using a $V_{M1\text{-}M2}$ = 150 μV excitation as a function of electrostatic gates V_{G1} and V_{G2}, where V_{G1} and V_{G2} are connected for each corresponding section of the device. (b) Measured photovoltage response as a function of V_{G1} and V_{G2} using a CO_2 laser excitation (280 μW, f_{mod} = 100 Hz). (c) Measured responsivity (R_V) at (V_{G1} = 5 V and V_{G2} = 30 V) as a function of modulation frequency (f_{mod}). Blue squares represent experimentally measured value. Red line represents fitting of data to eq S1.3 with an extracted time constant of τ_{th} = 23 ms. The inset shows the percent optical transmission of the substrate (τ_{SiN}) as a function of wavelength (λ).

aperture that was illuminated by a blackbody source (T_0 = 472 K) and scanned in the IM1 plane using a series of linear actuators (Thorlabs). Figure 3d,e shows the measured magnitude and phase of the photovoltage response as a function of scan position (step size = 0.5 mm for x and y). The image shown clearly reproduces the starting aperture; however, the image's spatial resolution is limited mainly by the step size of the scan, rather than the detector.

To evaluate the technological applications of this type of detector, the ultimate intrinsic performance of these graphene-based devices is evaluated. A common figure of merit for comparing various thermal detectors is detectivity (D^*). Assuming a thermo-electric detection mechanism and the device is Johnson noise limited,[1,19,22] the material-dependent components of D^* are the Seebeck coefficient (S) and the bulk resistivity (ρ_{sh}) (eq 1), ignoring emissivity (ε) for now since the optical absorption is assumed to be done by the membrane or absorbing material, which is different than the sensing material

$$D^*_{\text{thermopile}} \propto \frac{S}{\sqrt{\rho_{sh}}} \qquad (1)$$

Figure 4a plots the Seebeck coefficient versus bulk resistivity for a variety of common thermo-electric materials.[1,23] To compare graphene's 2D resistivity to other 3D materials, we have assumed stacked complementary doped layers of graphene, which could be achieved either through complementary chemical doping or electrostatically gated stacked graphene/h-BN/graphene capacitors. Because graphene's carrier concentration (n_s) is controlled via applied gate voltages, S and ρ_{sh} vary as a function of n_s (see Supporting Information). By modeling the effect of nonidealities on the Seebeck coefficient of graphene,[24] the fixed charge impurity concentration (n_0) limits the Seebeck

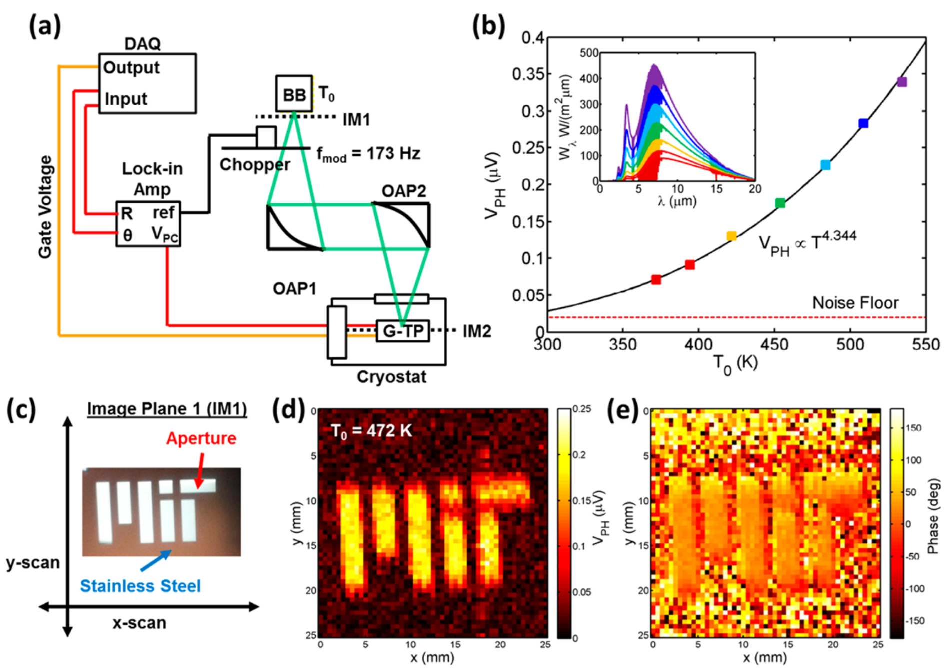

Figure 3. Thermal detection using graphene thermopile. (a) Experimental schematic. Two off-axis parabolic (OAP) mirrors are used to transfer infrared energy from the blackbody (BB) source to the device under testing (G-TP, number of junctions = 1). (b) Measured photovoltage (V_{PH}) as a function of blackbody temperature (T_0), using a calibrated blackbody source. Black line represents power law fitting of temperature dependence of the measured photovoltage ($V_{PH} = \beta T_0^{\alpha}$, α = 4.334, $\beta = 5 \times 10^{-13}$ V/K^4). The measured noise floor of the system is 0.02 μV at f_{mod} = 173 Hz. The inset shows the estimated infrared energy emitted as a function of blackbody temperature including atmospheric transmission, each color corresponding to the points on the main plot. The estimated blackbody power incident on the device is 23 μW at 536 K. (c) The thermal image was formed by placing a laser cut stainless steel aperture in front of the blackbody source (T = 472 K, f_{mod} = 173 Hz) and scanned in position using a series of motorized X−Y translation stages. The magnitude (d) and phase (e) of the measured signal are shown as a function of actuator position. The step size was 0.5 mm, and the integration time was 3 s per pixel.

DOI: 10.1021/acs.nanolett.5b01755
Nano Lett. 2015, 15, 7211−7216

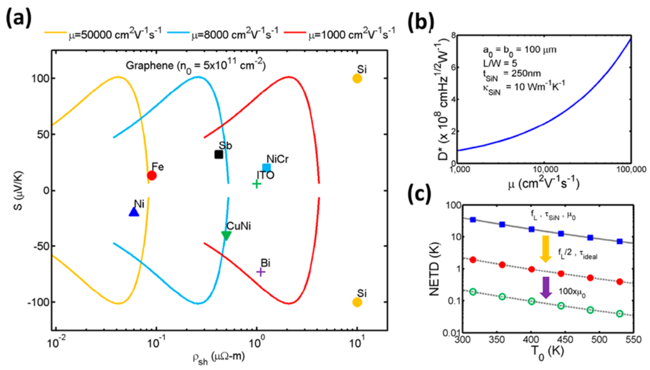

Figure 4. Performance analysis of graphene thermopile. (a) Plot of graphene Seebeck coefficient (S) as a function of bulk resistivity (ρ_{sh}). Graphene Seebeck coefficient and resistance are computed utilizing a square-root charge model assuming various values of carrier mobility (μ = 1000, 8000, 50 000 cm^2 V^{-1} s^{-1}) and a charge impurity at the charge neutrality point of $n_0 = 5 \times 10^{11}$ cm^{-2}. (b) Computed detectivity (D^*) of a graphene thermopile assuming a device area (A_0) = 100 × 100 μm^2, a thermal isolation leg with an aspect ratio of L/W of 5, thickness of thermal isolation membrane of 250 nm, and a thermal conductivity of 10 W m^{-1} K^{-1}. (c) Noise equivalent temperature difference (NETD) computed directly from experimental data from Figure 3b: (blue squares) with a focal length (f_L) of 50.8 mm, optical absorption of silicon nitride (τ_{SiN}) from Figure 2c, and starting mobility (μ_0) from Figure 2a. Red circles indicate the expected improvement in NETD due to reducing the focal length by a factor of 2, as well as assuming a 100% optical absorption (τ_{ideal}) after atmospheric and window (ZnSe) transmission. The green open circles represent the additional change to NETD of the red circles due to improving the quality of the graphene mobility by 100×.

coefficient for graphene, while μ limits the resistivity of graphene (see Supporting Information). However, while D^* depends on the ratio of $S/\sqrt{\rho_{sh}}$, for graphene, $D^*_{thermopile} \propto \sqrt{\mu}$ (see Supporting Information). Therefore, as shown in Figure 4a, high mobility graphene (μ > 10 000 cm^2 V^{-1} s^{-1}) can actually outperform other thermocouple materials, even conventional silicon based thermopiles (see Supporting Information).[1,23] Figure 4b plots D^* versus μ for a graphene thermopile assuming standard device parameters (see Table 1). The achievable range of D^*

Table 1. Device Simulation Parameters

parameters	units	value
κ_{SiN}	W m^{-1} K^{-1}	10
c_{SiN}	J g^{-1} K^{-1}	0.17
ρ_{SiN}	kg m^{-3}	2500
t_{SiN}	nm	250
a_0	μm	100
b_0	μm	100
L/W		5
N		1
N_{layers}		1

is 2–8 × 10^8 cm Hz$^{1/2}$ W^{-1} for a single monolayer of graphene is already on par or superior to comparable sized thermopile devices assuming electrical noise limited devices.[25−27] While D^* allows us to compute the intrinsic material-dependent sensitivities of these detectors, the imaging system's ability to differentiate between various blackbodies is better captured by a different figure of merit: noise equivalent temperature difference (NETD) shown in eq 2

$$\mathrm{NETD}(T_0) = \left.\frac{V_{\text{noise floor}}}{\frac{\mathrm{d}V_{PH}(T)}{\mathrm{d}T}}\right|_{T_0} \propto \frac{{f_L}^2}{\tau D^*} \quad (2)$$

where τ is the total integrated optical absorption in the absorber region and f_L is the focal length. Using eq 2 and Figure 3b, the experimentally measured NETD of our system is 30–40 K (Figure 4c, blue squares); however, this value only sets an upper bound for the minimal NETD. Equation 2 also shows how NETD is dependent on other external factors of the system including both the imaging optics and the optical absorption of the infrared absorber. Figure 4c (red circles) plots the improvement (×16–20) to the NETD simply by reducing the focal length from 50.8 mm to 25.4 mm and enhancing the optical absorption of the SiN to 100% (i.e., deposition of carbon black) (see Supporting Information).[28] While these extrinsic improvements can achieve a NETD of ∼1 K, the mobility of the graphene in our devices ∼100 cm^2 V^{-1} s^{-1} is still far from ideal due to doping, defects, and tears associated with transfer and device fabrication. However, improved transfer techniques in conjunction with h-BN[29] suggest a 100× improvement in carrier mobility of the graphene can easily be achieved, which results in an NETD of 30–150 mK, a value that can still be lowered through improvements to the thermal isolation. In spite of these possible routes for improvement, the measured NETD of our current device already suggests the possibility of resolving the thermal radiation of a human subject (∼320–330 K). Figure 5 shows the measured V_{PH} using a human hand as the thermal source instead of the calibrated blackbody source used earlier (Figure 5a). While a longer integration time (10 s) was necessary (potentially due to the variability in the position of the human hand), Figure 5b,c clearly shows that the detected presence and absence of the human hand in both the averaged phase and magnitude of V_{PH}. When the infrared radiation from a warm body is more than the ambient noise, the lock-in amplifier output tends to a constant value with a set phase. However, without a thermal source the phase of the output is unlocked and is a random value (−180°, 180°), which results in an averaged value of zero.

In conclusion, by integrating graphene technology with standard silicon MEMS fabrication, we are able to demonstrate real-world technological applications for graphene thermal imagers, imaging blackbody objects, and sensing and detecting human heat signatures. While these demonstrations have utilized current graphene technologies, improvements in graphene transfer and synthesis continue to rapidly advance, and graphene's ultimate detector performance can exceed conventional technologies due to graphene's unique high carrier transport, low thermal mass, and ambipolar band structure, which could be utilized for many other

DOI: 10.1021/acs.nanolett.5b01755
Nano Lett. 2015, 15, 7211−7216

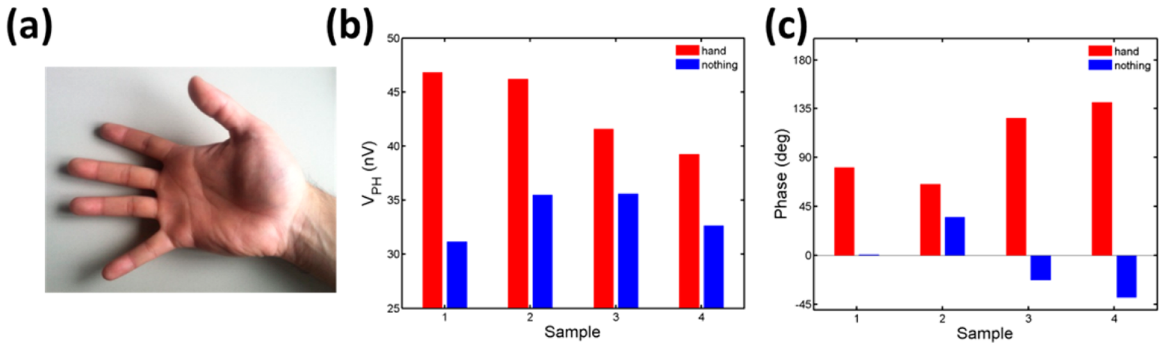

Figure 5. Thermal sensing from human target. (a) Picture of the human hand used as a thermal source and placed at the focal position of OAP1. The measured magnitude (b) and phase (c) of the photovoltage with and without the hand in place of the blackbody source are also shown. The integration time was 10 s per data sample with the lock-in and chopper wheel operating in both cases.

applications in the infrared including materials inspection or even biological applications. Furthermore, utilizing back end of the line (BEOL) compatible processes with complementary metal oxide semiconductor (CMOS) technology also suggests an easy process integration path for future graphene-thermopile based focal plane arrays (FPA).[25,30] While in this work we have used an electrostatically tunable thermocouple, complementary dopants (p and n type) applied to a single layer of graphene may also be sufficient for forming a thermal sensor, which given the optical transparency of both the SiN and the graphene could enabled stacked multiwavelength detectors.[31] Finally, given that doping graphene can be done very easily by tailoring the surrounding environment (such as spin on dopants), one could also imagine completely low temperature polymer based thermopiles where the thermal isolation could be formed from a simple casting/stamping, enabling extremely low cost and transparent sensors for thermal imaging and sensing applications.

■ ASSOCIATED CONTENT

Ⓢ Supporting Information

The Supporting Information is available free of charge on the ACS Publications website at DOI: 10.1021/acs.nanolett.5b01755.

> Details with regards to device fabrication, electrical and optical characterization systems, thermal time constant extraction, analysis of improvements due to thermal isolation by suspension, derivations for D^* and NETD for graphene, and comparison between graphene and silicon based thermopiles (PDF)

■ AUTHOR INFORMATION

Corresponding Authors

*E-mail: pjarillo@mit.edu.
*E-mail: tpalacios@mit.edu.

Author Contributions

A.L.H and P.K.H. contributed equally to this work

Notes

The authors declare no competing financial interest.

■ ACKNOWLEDGMENTS

This work has been supported in part by MIT/Army Institute for Soldier Nanotechnologies, Army Research Laboratories, Office of Naval Research GATE-MURI program, Solid State Solar Energy Conversion Center (S^3TEC), MIT Center for Integrated Circuits and Systems, and Air Force Office of Scientific Research. Sample fabrication was performed at the MIT Microsystems Technology Laboratories and NanoStructure Laboratories in the Research Lab of Electronics (NSL-RLE). J.K. also acknowledges the STC Center for Integrated Quantum Materials, NSF Grant No. DMR-1231319.

■ REFERENCES

(1) Rogalski, A. *Infrared Detectors*; CRC Press: Boca Raton, FL, 2000.
(2) Mueller, T.; Xia, F.; Avouris, P. Graphene photodetectors for high-speed optical communications. *Nat. Photonics* **2010**, *4*, 297−301.
(3) Bonaccorso, F.; Sun, Z.; Hasan, T.; Ferrari, A. C. Graphene photonics and optoelectronics. *Nat. Photonics* **2010**, *4*, 611−622.
(4) Konstantatos, G.; et al. Hybrid graphene-quantum dot phototransistors with ultrahigh gain. *Nat. Nanotechnol.* **2012**, *7*, 363−368.
(5) Fei, Z.; et al. Gate-tuning of graphene plasmons revealed by infrared nano-imaging. *Nature* **2012**, *487*, 82−85.
(6) Koppens, F. H. L.; Chang, D. E.; García de Abajo, F. J. Graphene Plasmonics: A Platform for Strong Light−Matter Interactions. *Nano Lett.* **2011**, *11*, 3370−3377.
(7) Lai, K. W. C.; Xi, N.; Chen, H.; Fung, C. K. M.; Chen, L. Development of graphene-based optical detectors for infrared sensing applications. *2011 IEEE Sensors* **2011**, 398−401.
(8) Herring, P. K.; et al. Photoresponse of an Electrically Tunable Ambipolar Graphene Infrared Thermocouple. *Nano Lett.* **2014**, *14*, 901−907.
(9) Karasik, B. S.; McKitterick, C. B.; Prober, D. E. Monolayer graphene bolometer as a sensitive far-IR detector. *Proc. SPIE* **2014**, *9153*, 915309−9.
(10) Yan, J.; et al. Dual-gated bilayer graphene hot-electron bolometer. *Nat. Nanotechnol.* **2012**, *7*, 472−478.
(11) Cai, X.; et al. Sensitive room-temperature terahertz detection via the photothermoelectric effect in graphene. *Nat. Nanotechnol.* **2014**, *9*, 814−819.
(12) Fong, K. C.; Schwab, K. C. Ultrasensitive and Wide-Bandwidth Thermal Measurements of Graphene at Low Temperatures. *Phys. Rev. X* **2012**, *2*, 031006.
(13) Han, Q. Highly sensitive hot electron bolometer based on disordered graphene. *Sci. Rep.* **2013**, *3*, 2533.
(14) Ryzhii, V.; et al. Graphene terahertz uncooled bolometers. *J. Phys. D: Appl. Phys.* **2013**, *46*, 065102.
(15) Alonso-González, P.; et al. Controlling graphene plasmons with resonant metal antennas and spatial conductivity patterns. *Science* **2014**, *344*, 1369−1373.
(16) Brar, V. W.; Jang, M. S.; Sherrott, M.; Lopez, J. J.; Atwater, H. A. Highly Confined Tunable Mid-Infrared Plasmonics in Graphene Nanoresonators. *Nano Lett.* **2013**, *13*, 2541−2547.
(17) Low, T.; Avouris, P. Graphene Plasmonics for Terahertz to Mid-Infrared Applications. *ACS Nano* **2014**, *8*, 1086−1101.
(18) Vicarelli, L.; et al. Graphene field-effect transistors as room-temperature terahertz detectors. *Nat. Mater.* **2012**, *11*, 865−871.
(19) Gabor, N. M.; et al. Hot Carrier−Assisted Intrinsic Photoresponse in Graphene. *Science* **2011**, *334*, 648−652.

(20) Song, J. C. W.; Rudner, M. S.; Marcus, C. M.; Levitov, L. S. Hot Carrier Transport and Photocurrent Response in Graphene. *Nano Lett.* **2011**, *11*, 4688−4692.
(21) Stark, I.; Stordeur, M.; Syrowatka, F. Thermal conductivity of thin amorphous alumina films. *Thin Solid Films* **1993**, *226*, 185−190.
(22) Xu, X.; Gabor, N. M.; Alden, J. S.; van der Zande, A. M.; McEuen, P. L. Photo-Thermoelectric Effect at a Graphene Interface Junction. *Nano Lett.* **2010**, *10*, 562−566.
(23) Sze, S. M. *Semiconductor Sensors*; Wiley-VCH: New York, 1994.
(24) Kim, S.; et al. Realization of a high mobility dual-gated graphene field-effect transistor with Al2O3 dielectric. *Appl. Phys. Lett.* **2009**, *94*, 062107.
(25) Oliver, A. D.; Wise, K. D. A 1024-element bulk-micromachined thermopile infrared imaging array. *Sens. Actuators, A* **1999**, *73*, 222−231.
(26) Schaufelbuhl, A.; et al. Uncooled low-cost thermal imager based on micromachined CMOS integrated sensor array. *J. Microelectromech. Syst.* **2001**, *10*, 503−510.
(27) Foote, M. C.; Jones, E. W.; Caillat, T. Uncooled thermopile infrared detector linear arrays with detectivity greater than 109 cmHz1/2/W. *IEEE Trans. Electron Devices* **1998**, *45*, 1896−1902.
(28) Fei, Z.; et al. Infrared Nanoscopy of Dirac Plasmons at the Graphene−SiO2 Interface. *Nano Lett.* **2011**, *11*, 4701−4705.
(29) Dean, C. R.; et al. Boron nitride substrates for high-quality graphene electronics. *Nat. Nanotechnol.* **2010**, *5*, 722−726.
(30) Gan, X.; et al. Chip-integrated ultrafast graphene photodetector with high responsivity. *Nat. Photonics* **2013**, *7*, 883−887.
(31) Liu, N.; et al. Large-Area, Transparent, and Flexible Infrared Photodetector Fabricated Using P-N Junctions Formed by N-Doping Chemical Vapor Deposition Grown Graphene. *Nano Lett.* **2014**, *14*, 3702.

DOI: 10.1021/acs.nanolett.5b01755
Nano Lett. 2015, 15, 7211−7216